WARNING CONCERNING COPYRIGHT RESTRICTIONS

Computational study of cold ions trapped in a double-well potential

Dmytro Shyshlov & Dmitri Babikov

Taylor & Francis
Taylor & Francis Group

Check for updates

RESEARCH ARTICLE

Computational study of cold ions trapped in a double-well potential

Dmytro Shyshlov and Dmitri Babikov

Chemistry Department, Marquette University, Milwaukee, USA

ABSTRACT

We report a rigorous computational treatment of quantum dynamics of cold ions in a double-well trap using the time-dependent Schrödinger equation. Our method employs a numerically accurate approach that avoids approximations, such as assumption of weak coupling between the wells; normal mode nature of vibrations; or harmonic approximation for energy spectrum of the double-well system. Our goal is to reproduce, from first principles, the process of energy swaps between the wells observed in the experiments at NIST [Nature **471**, 196 (2011)] and Innsbruck [Nature **471**, 200 (2011)]. The model parameters and the initial conditions are carefully chosen to mimic experimental conditions. We obtain accurate energies and wave functions of the system numerically, and study the evolution of motional wave packets to provide new insight. This model reproduces experimental results obtained by NIST and Innsbruck in detail. We explain the energy transfer in terms of wave packet dynamics in the asymmetric potential energy well. We also show that, for a localised initial wave packet, this phenomenon can be interpreted using the terms of classical dynamics, such as trajectory of motion governed by the well-known simple principle: the angle of reflection equals the angle of incidence.
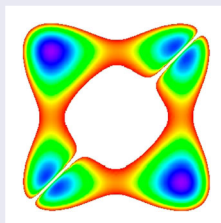
1. Introduction

In a typical ion-cooling and trapping experiment [1–5] a string of multiple ions is confined along the axis of the trap. Each ion interacts strongly with its neighbouring ions, and with the potential of the trap, which leads to the collective vibrational motion of the quasi-linear ion-string. The typical ion-ion distance in such architecture is on the order of a few micron, and the trapping potential is perfectly parabolic (harmonic) at this length-scale. Several ions, up to 9 per trap [6,7], can be trapped, cooled and entangled, to create a quantum information register/processor [2,4,8–14]. Further scaling can be achieved by combining several traps and shuttling individual ions between the traps [15–18].

An alternative approach to the ion trapping involves a strongly-anharmonic double-well trapping potential that is created along the axis of the trap:

$$V(z) = \beta z^4 - \alpha z^2. \qquad (1)$$

In recent years this approach was explored, both experimentally [19,20] and computationally [21,22]. The goal of the experiments was to keep the ions in two separate wells, at a significant distance, in order to reduce their Coulomb interaction and create two, almost independent, weakly-coupled quantum oscillators. This is qualitatively illustrated by Figure 1(a) for the case of two trapped ions, one in each well of the double-well trap. Using this architecture, the ion-ion distance can exceed 50 microns. The experiments conducted at NIST [19] and Innsbruck [20] used Be^+ and Ca^+ ions, respectively. Other properties of their traps are listed in Table 1. Note that in each case the potential barrier between the
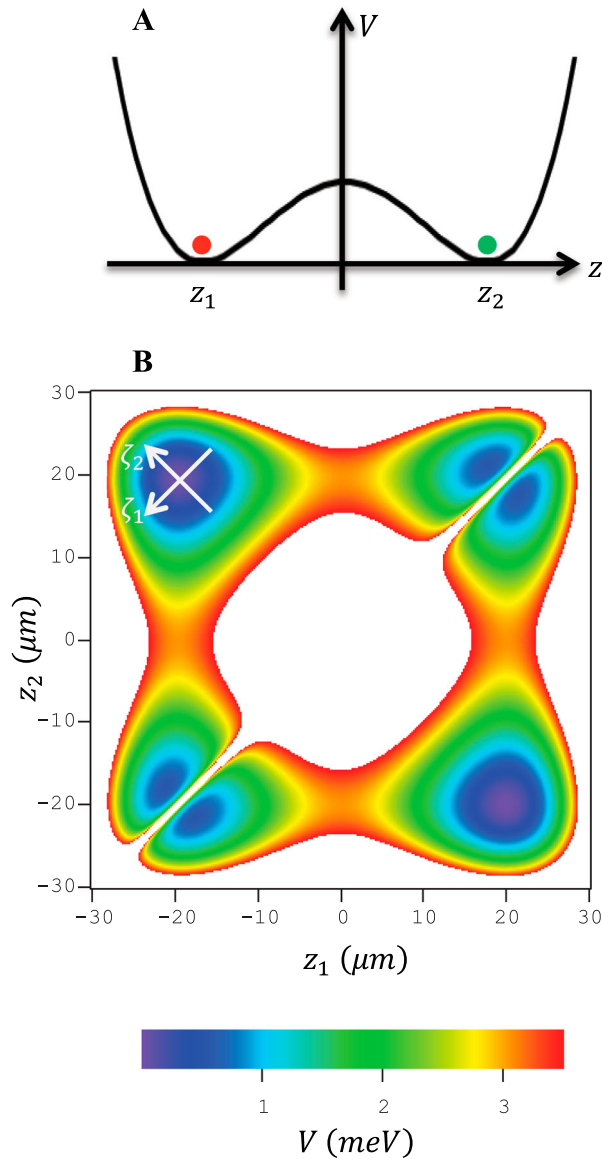
Figure 1. (a) Qualitative illustration of the double-well potential with two ions trapped in the separated wells; (b) Two-dimensional PES of the system in the Be^+ experiment. Two white axis inserted in the top left corner indicate the normal mode coordinates.

if the vibrational excitation is low (say within 10 quanta), the dynamics of the ion motion in two wells should be entirely independent. However, both NIST and Innsbruck groups observed very substantial transfer of the vibrational energy from one well to another, in spite of the seemingly weak coupling [19,20].

The goal of our paper is to understand this interesting result by modelling the quantum dynamics of the system of two ions in the double-well potential as accurately as possible, without making any assumptions concerning the coupling strength or the energy spectrum of the double-well system. Such rigorous theoretical tools, including construction of the potential energy surface of the system and normal mode analysis, are often used by molecular physicists [21,22]. First, we consider an accurate potential energy surface of the system, without a Taylor series expansion of the Coulomb interaction, and without truncating any higher-order terms. Then we numerically search for the minimum energy point on the surface and perform the normal mode analysis. We avoid harmonic approximation and use the normal mode frequencies only to set up an efficient basis set for accurate representation of the wave function. Then we compute and numerically diagonalise the Hamiltonian matrix to determine accurate eigenstates of the system (energies and wave functions). These eigenstates are used to study evolution of the vibrational wave packets in time and space. Initial conditions are choosen to mimic the experiments conducted at NIST and Innsbruck [19,20].

2. Theory

2.1. Parameters of the model

A combination of terms of the second and fourth orders, as in Equation (1), where α and β are two parameters, describes the double-well trap potential. One of the goals of our computational work is to reproduce experimental results by calculations, which requires an appropriate choice of α and β. Unfortunately, they are not directly measurable in the experiment. So, we have to find the

wells is very high. Simple estimates indicate that each well can maintain on the order of 10^5 quanta of the motional/vibrational excitation. One could expect that,

Table 1. Parameters of the double-well potential and comparison of the system properties in our model with those in the experiments of Ref. [19] and [20].

		Be^+ experiment		Ca^+ experiment	
		Measured [19]	Model	Measured [20]	Model
$\alpha \cdot 10^3$, meV/μm^2		—	15.525	—	1.167
$\beta \cdot 10^7$, meV/μm^4		—	205.3	—	8.525
Ion-ion distance d, μm		40	38.920	54	52.546
Potential barrier V_0, meV		3	2.935	0.5	0.399
Normal mode frequency, kHz	$\omega_1/2\pi$	4111.8	4111.375	540	536.928
	$\omega_2/2\pi$	4114.9	4114.600	543	539.177
Mode splitting $\delta\omega/2\pi$, kHz		3.226	3.22515	2.25	2.249
Energy swap time τ_{swp}, μs		155	155.11	222	222.25

values of the parameters α and β that reproduce other measurable characteristics of the experiment, such as equilibrium distance between the ions d, height of the potential barrier between the ions V_0, and most importantly, the system frequencies ω_1 and ω_2. These can be described by the average frequency $\omega_{ave} = (\omega_1 + \omega_2)/2$ and the splitting $\delta\omega = \omega_2 - \omega_1$.

For this, we carried out calculations of d, V_0, ω_{ave} and $\delta\omega$ (as explained in the next section) using different values of α and β. We considered 20 values of α and 20 values of β, covering 400 combinations in total, for both the Be^+ and Ca^+ experiments. Then we analysed the two-dimensional functions $d(\alpha, \beta)$, $V_0(\alpha, \beta)$, $\omega_{ave}(\alpha, \beta)$ and $\delta\omega(\alpha, \beta)$ using their contour plots and tried to identify the values of α and β that reproduce all four experimental characteristics.

For example, in Figure 2(a) one contour line (green) is given for the equilibrium distance of ions, d, dependent upon α and β to represent the experimental value of $d = 40\,\mu m$ in the Be^+ experiment. This line shows a significant slope, which indicates that the equilibrium ion-ion distance d is quite sensitive to both α and β, and that a number of combinations of α and β over a broad range of values can reproduce the experimental value of d.

Likewise, we plotted one contour line of the (α, β)-dependence at the experimental value of $V_0 = 3\,meV$ (light blue), one contour line for $\omega_{ave} = 2\pi \times 4.113\,MHz$ (dark blue) and one contour line for $\delta\omega = 2\pi \times 3.226\,kHz$ (red) in the Be^+ experiment. All four lines are shown together in Figure 2(a). We see that different pairs of curves intersect (six points total) which means that we can identify the values of α and β that will reproduce exactly any two experimental characteristics, but not all four characteristics at the same time, simply because the four curves in Figure 2(a) do not intersect at the same point.

However, we can see that in the range of values $\alpha = 1.52 - 1.58 \times 10^2\,meV/\mu m^2$ and $\beta = 1.93 - 2.05 \times 10^5\,meV/\mu m^4$ all four curves pass close together. Furthermore, different experimental characteristics differ in their importance and accuracy [19]. Namely, the vibration frequencies are measured more accurately than the geometric parameters of the trap d and V_0. Because of this, we choose the values of α and β to reproduce nearly exactly the experimental values of ω_{ave} and $\delta\omega$, while we reproduce the values of d and V_0 approximately. The corresponding point in the (α, β)-space is indicated by the black dot in Figure 2(a) for the Be^+ experiment, and similarly, in Figure 2(b) for the Ca^+ experiment. The values of α and β chosen for the model are listed in the Table 1. Deviations of the model values of d and V_0 from the experiment can also be estimated using Table 1. Thus, in the case of Be^+ experiment we have approximately three
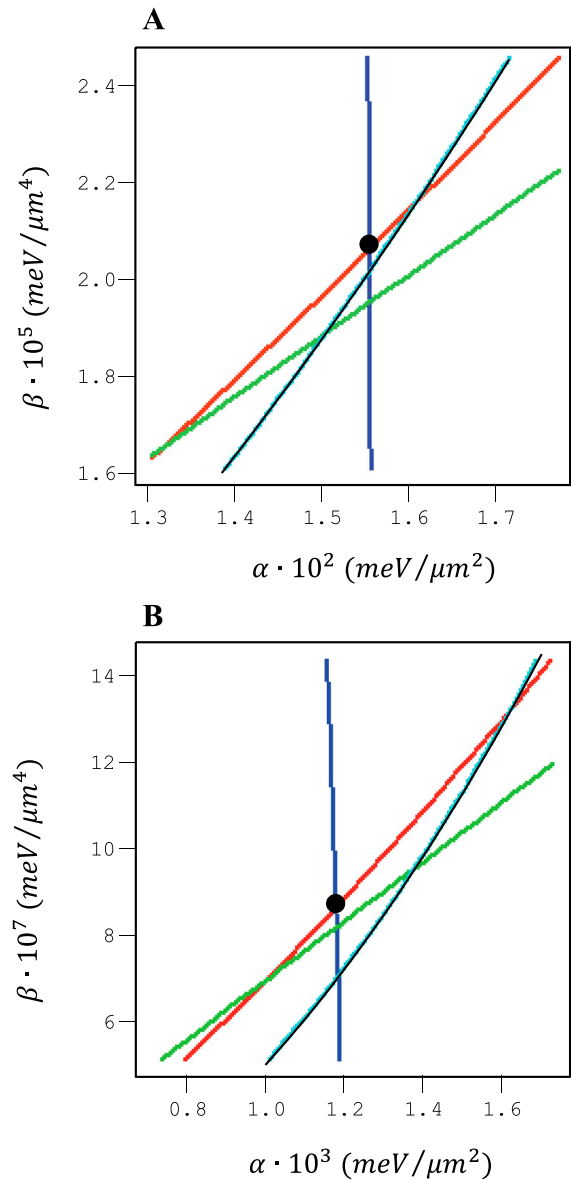
Figure 2. Dependence of system properties on parameters of the double-well potential in the cases of: (a) Be^+ experiment; and (b) Ca^+ experiment. In each case only one contour line is given that corresponds to the experimental value of the distance between ions d (green), potential barrier V_0 (cyan), average vibration frequency ω_{ave} (blue), and frequency splitting $\delta\omega$ (red). Black dot indicates the values of potential parameters α and β that were chosen to represent the trap in our model. (Colour online.)

percent deviation of the distance d and approximately two percent deviation of the potential barrier V_0. In the case of Ca^+ experiment we have approximately three percent deviation of d and approximately 20% deviation of V_0. Larger deviation of the potential barrier V_0 in the case of Ca^+ can be explained by the fact that the experimental value was not really reported in the paper by the Innsbruck group [20]. We derived it approximately from the schematic plot in that paper. All of our model parameters appear to be within experimental ranges of accuracy.

2.2. Hamiltonian of the system

When the trap parameters have been chosen, the potential energy of two ions in the double-well potential can be expressed as follows (in atomic units):

$$V(z_1, z_2) = \beta z_1^4 - \alpha z_1^2 + \beta z_2^4 - \alpha z_2^2 + \frac{1}{|z_2 - z_1|}, \quad (2)$$

where z_1 and z_2 are Cartesian coordinates of the ions along the axis of the trap. Equation 2 represents a two-dimensional potential energy surface (PES) of the system, $V(z_1, z_2)$. Such PES for the Be^+ experiment is visualised in Figure 1(b) using a colour map. It is symmetric with respect to the line $z_1 = z_2$ where the energy is infinite, due to Coulomb repulsion of two ions sitting in the same position. Overall, there are six potential energy wells on the PES. Two global minima correspond to the case of two ions sitting in two different wells, one ion per well. Two possibilities arise from the permutation of the two ions, either $z_1 < z_2$ or $z_1 > z_2$. Four local minima at higher energies correspond to both ions sitting in the same well. These four possibilities arise from the permutations and the presence of two wells. The PES for the Ca^+ experiment exhibits similar features. The ions in the trap never swap, meaning that the symmetry consequences of the ion-ion exchange need not be considered here.

We focus on the global minimum in the top left corner of Figure 1(b) to perform the normal mode analysis corresponding to $z_1 < z_2$ (first ion to the left, second ion to the right). As a first step, we need to find the equilibrium coordinates of the ions z_{e1} and z_{e2} that correspond to this global minimum, which cannot be done analytically. To perform numerical minimisation we employ the Newton–Raphson method [23] which results in $(z_{e1}, z_{e2}) = (-19.46\,\mu m, 19.46\,\mu m)$ for the Be^+ experiment and $(z_{e1}, z_{e2}) = (-26.27\mu m, 26.27\mu m)$ for the Ca^+ experiment. The values of potential energy at the minimum were $V^{eq} = -5.8331 meV$ for the Be^+ experiment and $V^{eq} = -0.7713 meV$ for the Ca^+ experiment.

At the stationary point we can perform the normal mode analysis. Both experiments considered here use the ions of identical masses (either two Be^+, or two Ca^+ ions). Therefore, the mass-weighted Hessian matrix can be written as:

$$F = \begin{vmatrix} m & 0 \\ 0 & m \end{vmatrix}^{-\frac{1}{2}} \begin{vmatrix} \frac{\partial^2 V}{\partial z_1^2} & \frac{\partial^2 V}{\partial z_1 \partial z_2} \\ \frac{\partial^2 V}{\partial z_1 \partial z_2} & \frac{\partial^2 V}{\partial z_2^2} \end{vmatrix} \begin{vmatrix} m & 0 \\ 0 & m \end{vmatrix}^{-\frac{1}{2}}. \quad (3)$$

From Equation (2), and taking into account that $z_1 < 0$ and $z_2 > 0$, the elements of the matrix are computed analytically:

$$\frac{\partial^2 V}{\partial z_{1,2}^2} = -2\alpha + 12\beta z_{1,2}^2 + \frac{2}{(z_2 - z_1)^3}, \quad (4a)$$

$$\frac{\partial^2 V}{\partial z_1 \partial z_2} = -\frac{2}{(z_2 - z_1)^3}. \quad (4b)$$

Using Equations (3) and (4) matrix F at the equilibrium point (z_{e1}, z_{e2}) is obtained:

$$F = \frac{1}{m} \begin{vmatrix} -2\alpha + 12\beta z_{e1}^2 + \frac{2}{(z_{e2}-z_{e1})^3} & -\frac{2}{(z_{e2}-z_{e1})^3} \\ -\frac{2}{(z_{e2}-z_{e1})^3} & -2\alpha + 12\beta z_{e2}^2 + \frac{2}{(z_{e2}-z_{e1})^3} \end{vmatrix}. \quad (5)$$

Diagonalization of this matrix produces the frequencies ω_1 and ω_2 of the normal modes (reported in Table 1) and their corresponding eigenvectors:

$$A = \begin{vmatrix} -\frac{\sqrt{2}}{2} & -\frac{\sqrt{2}}{2} \\ -\frac{\sqrt{2}}{2} & \frac{\sqrt{2}}{2} \end{vmatrix}. \quad (6)$$

The first column of matrix A corresponds to the centre-of-mass motion mode, $\Delta z_1 = \Delta z_2$, while the second column corresponds to the symmetric stretching mode, $\Delta z_1 = -\Delta z_2$. Here we defined displacements of ions from their equilibrium positions as:

$$\Delta z_1 = z_1 - z_{e1}, \ \Delta z_2 = z_2 - z_{e2}. \quad (7)$$

Using a harmonic model, we can predict an approximate energy spectrum of the system with the normal mode frequencies ω_1 and ω_2. Table 2 shows these results for both experiments with Be^+ and Ca^+ ions, respectively.

The Hamiltonian of the system is written initially in Cartesian coordinates as:

$$\hat{H}(z_1, z_2) = -\frac{1}{2m}\frac{\partial^2}{\partial z_1^2} - \frac{1}{2m}\frac{\partial^2}{\partial z_2^2} + V(z_1, z_2) - V^{eq}, \quad (8)$$

where $V(z_1, z_2)$ is the potential energy surface from Equation (2) and V^{eq} is the potential energy values of equilibrium configuration. In order to study the dynamics of the system near the equilibrium point it is convenient, instead of Cartesian coordinates (z_1, z_2), to employ the mass unscaled normal mode coordinates (ζ_1, ζ_2) defined as:

$$\begin{pmatrix} \zeta_1 \\ \zeta_2 \end{pmatrix} = A^T \begin{pmatrix} \Delta z_1 \\ \Delta z_2 \end{pmatrix}, \quad (9)$$

where A^T is transposed matrix A from Equation (6). Coordinate ζ_1 describes the centre-of-mass motion mode and coordinate ζ_2 describes the symmetric stretching mode as shown in Figure 1(b). From Equations (7–9) the Hamiltonian operator in the normal mode coordinates

Table 2. Predicted energy spectra of two ions in the double-well experiments of Ref. [19,20].

Energy level	Normal mode assignment (n_1, n_2)	Be$^+$ experiment, kHz		Ca$^+$ experiment, kHz	
		Harmonic approximation	Matrix diagonalization	Harmonic approximation	Matrix diagonalization
1	(0,0)	4112.9875	4112.9860	538.05245	538.05227
2	(1,0)	8224.3623	8224.3564	1074.9800	1074.9793
3	(0,1)	8227.5875	8227.5816	1077.2298	1077.2290
4	(2,0)	12335.7372	12335.7247	1611.9076	1611.9061
5	(1,1)	12338.9624	12338.9476	1614.1573	1614.1556
6	(0,2)	12342.1875	12342.1750	1616.4071	1616.4056
7	(3,0)	16447.1121	16447.0907	2148.8352	2148.8326
8	(2,1)	16450.3372	16450.3114	2151.0849	2151.0818
9	(1,2)	16453.5624	16453.5366	2153.3346	2153.3316
10	(0,3)	16456.7876	16456.7662	2155.5844	2155.5818

can be derived:

$$\hat{H}(\zeta_1, \zeta_2) = -\frac{1}{2m}\frac{\partial^2}{\partial \zeta_1^2} - \frac{1}{2m}\frac{\partial^2}{\partial \zeta_2^2} + V(\zeta_1, \zeta_2) - V^{eq},$$
(10)

$$V(\zeta_1, \zeta_2) = \beta\left(z_{e1} - \frac{\zeta_1 + \zeta_2}{\sqrt{2}}\right)^4 - \alpha\left(z_{e1} - \frac{\zeta_1 + \zeta_2}{\sqrt{2}}\right)^2$$
$$+ \beta\left(z_{e2} + \frac{\zeta_2 - \zeta_1}{\sqrt{2}}\right)^4$$
$$- \alpha\left(z_{e2} + \frac{\zeta_2 - \zeta_1}{\sqrt{2}}\right)^2 + \frac{1}{\left|\sqrt{2}\zeta_2 + z_{e2} - z_{e1}\right|}.$$
(11)

Note that the Coulomb term in Equation (11) depends on the symmetric stretching coordinate ζ_2 only, and does not depend on ζ_1, which is consistent with the property that the centre-of-mass motion, described by ζ_1, does not change the distance between the ions. By removing parentheses in Equation (11) one can easily check that the potential $V(\zeta_1, \zeta_2)$ contains the coupling terms between the two vibration modes and therefore is non-separable.

We stress that the representation of the Hamiltonian operator in the normal mode coordinates is not an approximation of any sort, but an exact mathematical transformation used to establish a convenient and efficient basis set. We do not make any assumptions for the normal mode character of the spectrum, or for separability of the PES in these coordinates.

2.3. Basis set expansion and matrix diagonalization

A direct-product basis set expansion is used to represent wave functions of the system:

$$\psi^\nu(\zeta_1, \zeta_2) = \sum_{i,j}^N c_{ij}^\nu \varphi_i(\zeta_1)\varphi_j(\zeta_2),$$
(12)

where $\varphi_i(\zeta_1)$ and $\varphi_j(\zeta_2)$ are one-dimensional basis sets for the normal mode coordinates ζ_1 and ζ_2, while N is the number of basis functions, index ν labels states of the two-ion system and has values in the range from 1 to N^2, c_{ij}^ν are coefficients of linear combination. For each coordinate we employ the basis set of eigenfunctions of the harmonic oscillator with its corresponding normal mode frequency:

$$\varphi_j(\zeta_{1,2}) = A_j \cdot e^{-y_{1,2}^2} \cdot H_j(y_{1,2}),$$
(13a)

$$A_j = \frac{1}{\sqrt{2^j j!}}\left(\frac{m\omega_{1,2}}{\pi}\right)^{1/4}.$$
(13b)

Here $\omega_{1,2}$ are the frequencies of the normal modes, H_j are Hermite polynomials. The standard notations are used: $y_{1,2} = \gamma_{1,2}\zeta_{1,2}$, where $\gamma_{1,2} = \sqrt{m\omega_{1,2}}$. The number of basis functions included in our calculations is $N = 40$ for each degree of freedom.

Elements of the Hamiltonian matrix should be calculated as:

$$H_{ij,kl} = \langle \varphi_i(\zeta_1)\varphi_j(\zeta_2)|\hat{H}|\varphi_k(\zeta_1)\varphi_l(\zeta_2)\rangle.$$
(14)

The kinetic energy part of the Hamiltonian matrix can be derived from Equations (10) and (14):

$$T_{ij,kl} = -\frac{1}{2m}\left\langle \varphi_i(\zeta_1)\varphi_j(\zeta_2)\left|\frac{\partial^2}{\partial\zeta_1^2} + \frac{\partial^2}{\partial\zeta_2^2}\right|\varphi_k(\zeta_1)\varphi_l(\zeta_2)\right\rangle$$
$$= -\frac{1}{2m}\delta_{jl}\left\langle \varphi_i(\zeta_1)\left|\frac{\partial^2\varphi_k(\zeta_1)}{\partial\zeta_1^2}\right.\right\rangle$$
$$- \frac{1}{2m}\delta_{ik}\left\langle \varphi_j(\zeta_2)\left|\frac{\partial^2\varphi_l(\zeta_2)}{\partial\zeta_2^2}\right.\right\rangle$$
(15)

Second derivative of the basis functions can be calculated analytically from Equation (13):

$$\frac{\partial^2\varphi_k(\zeta_1)}{\partial\zeta_1^2} = A_k\left(\frac{\partial^2 H_k(y_1)}{\partial\zeta_1^2}\cdot e^{-y_1^2/2} + 2\frac{\partial H_k(y_1)}{\partial\zeta_1}\right.$$
$$\left.\cdot\frac{\partial}{\partial\zeta_1}(e^{-y_1^2/2}) + H_k(y_1)\cdot\frac{\partial^2}{\partial\zeta_1^2}(e^{-y_1^2/2})\right)$$
(16)

Derivatives of Hermite polynomials can be calculated using the property:

$$H'_k(y_1) = 2kH_{k-1}(y_1). \qquad (17)$$

From Equation (17) we can obtain:

$$H'_k(y_1) = \gamma_1 H'_k(\gamma_1 \zeta_1) = \gamma_1 \cdot 2kH_{k-1}(\gamma_1 \zeta_1), \qquad (18)$$

$$H''_k(y_1) = (\gamma_1 H'_k(\gamma_1 \zeta_1))' = 2k\gamma_1 (H_{k-1}(\gamma_1 \zeta_1))'$$
$$= 4k(k-1)\gamma_1^2 H_{k-2}(\gamma_1 \zeta_1). \qquad (19)$$

Substituting Equations (16,18, and 19) into Equation (15) we obtain the final expression for matrix elements of the kinetic energy operator:

$$T_{ij,kl} = -\frac{1}{2m}\delta_{jl}\langle \varphi_i(\zeta_1)|A_k(4k(k-1)\gamma_1^2$$
$$\times H_{k-2}(\gamma_1 \zeta_1))e^{-\gamma_1^2 \zeta_1^2/2}\rangle$$
$$-\frac{1}{2m}\delta_{ik}\langle \varphi_j(\zeta_2)|A_l(4l(l-1)\gamma_2^2$$
$$\times H_{l-2}(\gamma_2 \zeta_2))e^{-\gamma_2^2 \zeta_2^2/2}\rangle. \qquad (20)$$

Matrix elements of the potential energy operator are:

$$V_{ij,kl} = \langle \varphi_i(\zeta_1)\varphi_j(\zeta_2)|V(\zeta_1, \zeta_2)|\varphi_k(\zeta_1)\varphi_l(\zeta_2)\rangle. \qquad (21)$$

Integrals in Equations (20) and (21) are computed numerically using the Gauss-Hermite quadrature method [23]. The potential energy $V(\zeta_1, \zeta_2)$ is, again, not separable, so, we have to compute double integrals in Equation (21).

Diagonalization of the Hamiltonian matrix $\boldsymbol{H} = \boldsymbol{T} + \boldsymbol{V}$ numerically, using the DSYEV subroutine [24], produces an accurate energy spectrum of the system. Table 2 presents the resultant energy spectra for both Be$^+$ and Ca$^+$ experiments. For both systems, the energies predicted by harmonic approximation are very close to those obtained accurately by diagonalising the Hamiltonian matrix, with differences in the seventh significant figure.

In order to quantify anharmonicities of the system we fitted the lower ten energy levels of the accurate spectrum with a Dunham expansion:

$$E_{\nu_1 \nu_2} = D + \omega_1\left(\nu_1 + \frac{1}{2}\right) + \omega_2\left(\nu_2 + \frac{1}{2}\right)$$
$$- \Delta_1\left(\nu_1 + \frac{1}{2}\right)^2 - \Delta_2\left(\nu_2 + \frac{1}{2}\right)^2$$
$$- \Delta_{12}\left(\nu_1 + \frac{1}{2}\right)\left(\nu_2 + \frac{1}{2}\right). \qquad (22)$$

Table 3 gives the values of the fitted coefficients. Anharmonicites of the two normal modes, Δ_1 and Δ_2, are

Table 3. Coefficients of Dunham expansion (including intra- and inter-mode anharmonicities) obtained by fitting lower ten energy levels for the Be$^+$ and Ca$^+$ ions in the double-well traps.

	Be$^+$ experiment	Ca$^+$ experiment
$\omega_1/2\pi$, kHz	4111.375	536.928
$\omega_2/2\pi$, kHz	4114.600	539.177
$\Delta_1/2\pi$, Hz	1.0993	0.1292
$\Delta_2/2\pi$, Hz	1.1082	0.1339
$\Delta_{12}/2\pi$, Hz	0.18632	0.02364
$D/2\pi$, Hz	4.4278	0.5346
$\delta\omega/2\pi$, kHz	3.22515	2.249

very similar and tiny compared to the normal mode frequencies, $\Delta_{1,2} \sim 10^{-6}\omega_{1,2}$. This result is consistent with the data of Table 2. It appears that the spectrum of the system is very harmonic, at least at the level of low vibrational excitation (say, 10 quanta), in spite of the fact that the anharmonic Coulomb interaction is included exactly without any truncation. The reasons for this property are further discussed in Sec. 3. We would like to stress that we carried out a very detailed convergence study to ensure that accuracy of our predictions of the frequency values ($\sim 10^{-12}\omega$) is well below the magnitude of anharmonicities.

2.4. Time-evolution of the system

To model time-evolution of vibrational wave packets, the numerically accurate wave functions of the system $\psi^\nu(\zeta_1, \zeta_2)$ and the values of energies E_ν should be used. The time-dependent wave function of the system can be expressed as:

$$\psi^t(\zeta_1, \zeta_2) = \sum_\nu b^\nu \psi^\nu(\zeta_1, \zeta_2)e^{-iE_\nu t}, \qquad (23)$$

where b^ν are probability amplitudes determined by projecting the initial wave packet $\psi^{in}(\Delta z_1, \Delta z_2)$ onto eigenfunctions of the system:

$$b^\nu = \langle \psi^\nu(\zeta_1, \zeta_2)|\psi^{in}(\Delta z_1, \Delta z_2)\rangle. \qquad (24)$$

Integration of Equation (24) is carried out numerically using the Gauss-Hermite quadrature method [23]. When probability amplitudes b^ν are known, the time-dependent wave function of the system $\psi^{t=0}(\zeta_1, \zeta_2)$ can be propagated in time analytically using Equation (23).

3. Results and analysis

3.1. Initial state preparation

In the experiments the double-well potential is initially made asymmetric by applying an additional field in order to detune vibrational frequencies of the two wells and to effectively remove coupling between the motion of two

ions. The initial states of the ions are prepared by first Doppler cooling *both* ions and then by the subsequent sideband cooling only *one* of the ions. As a result, one ion (say #1) is produced in the lower vibrational state than the other ion (say #2). After that, the two potential wells are brought into resonance and the ions exchange vibrational energy. After time t, the resonance of the potential wells is removed and the vibrational state of the ion #1 is measured.

In order to model this experimental procedure, we have to consider the states of individual ions rather than the states of the overall system. These states of the individual ions are appropriately described by two *local* vibration modes (rather than normal modes) and they are characterised by displacement coordinates Δz_1 and Δz_2 for each well. The corresponding wave functions $\psi^{loc}(\Delta z_1)$ and $\psi^{loc}(\Delta z_2)$ are introduced for each well, and the initial state of the system in the experiment is defined as:

$$\psi^{in}(\Delta z_1, \Delta z_2) = \psi^{loc}(\Delta z_1)\psi^{loc}(\Delta z_2). \quad (25)$$

We use harmonic approximation to define the local mode states populated in the experiment. The shape of the PES in the vicinity of the minimum defines the local mode harmonic frequency ω_0 which is the same for the two wells:

$$\omega_0 = \sqrt{\frac{1}{m} \cdot \frac{\partial^2 V}{\partial z_1^2}} = \sqrt{\frac{1}{m} \cdot \frac{\partial^2 V}{\partial z_2^2}}. \quad (26)$$

In fact, ω_0 is a diagonal element of the Hessian matrix before we perform any diagonalization (see Equation (3)). The value of ω_0 is $2\pi \times 4112.988$kHz for the Be$^+$ and $2\pi \times 538.054$kHz for the Ca$^+$ experiments, respectively.

Initial conditions of the experiment are given in terms of the mean occupation numbers for each well [19,20] and that can be defined as:

$$\langle n_1 \rangle = \sum_i i \cdot a_i^2, \quad (27a)$$

$$\langle n_2 \rangle = \sum_j j \cdot a_j^2. \quad (27b)$$

At the initial moment of time in the Be$^+$ experiment $\langle n_1 \rangle = 0.35$ and $\langle n_2 \rangle = 2.3$, while in the Ca$^+$ experiment $\langle n_1 \rangle = 4$ and $\langle n_2 \rangle = 9$. Obviously, those values of mean occupations can be obtained with different combinations of the coefficients a_i and a_j, and the experimental distributions are not known. Here we test two methods of generating the initial conditions.

In the first method the initial wave function in each well is a coherent wave packet, a linear superposition of

small number of harmonic oscillator functions $\varphi^{loc}(\Delta z)$:

$$\psi^{loc}(\Delta z_1) = \sum_i a_i \varphi_i^{loc}(\Delta z_1), \quad (28a)$$

$$\psi^{loc}(\Delta z_2) = \sum_j a_j \varphi_j^{loc}(\Delta z_2). \quad (28b)$$

This gives the initial wave function of the system, expressed as:

$$\psi^{in}(\Delta z_1, \Delta z_2) = \sum_{i,j} a_{ij} \varphi_i^{loc}(\Delta z_1)\varphi_j^{loc}(\Delta z_2), \quad (29)$$

where $a_{ij} = a_i \cdot a_j$ are coefficients of the linear combination, determined by experimental conditions. This initial wave function $\psi^{in}(\Delta z_1, \Delta z_2)$ should be projected onto accurate eigenstates of the system $\psi^v(\zeta_1, \zeta_2)$ according to Equation (24), in order to determine the probability amplitudes b^v for the initial wave packet $\psi^{t=0}(\zeta_1, \zeta_2)$. Such projection can be easily computed, since the initial wave function expressed in the local mode coordinates is analytic. Its value can be determined at the same quadrature points in the (ζ_1, ζ_2)-space where the numeric wave function $\psi^{t=0}(\zeta_1, \zeta_2)$ should be defined.

We implemented this first method by setting up the initial conditions to include the *minimal* number of states into the coherent superposition of Equation (28): two states in each well, closest to the mean value. For example, to mimic the Be$^+$ experiment we set $a_{i=0}^2 = 0.7$ and $a_{i=1}^2 = 0.3$ to have $n_1 = 0.35$, whereas we set $a_{j=2}^2 = 0.65$ and $a_{j=3}^2 = 0.35$ to have $n_2 = 2.3$. This choice generates the following values of probability amplitudes for Equation (29): $a_{02} = \sqrt{0.7} \cdot \sqrt{0.65}$, $a_{12} = \sqrt{0.7} \cdot \sqrt{0.35}$, $a_{03} = \sqrt{0.3} \cdot \sqrt{0.65}$, and $a_{13} = \sqrt{0.3} \cdot \sqrt{0.35}$. All other amplitudes are set to zero. The resultant distribution of the initial state populations is illustrated by Figure 3(a).

In the second method we set up the *thermal* Boltzmann distribution of the initial states in each well, typical to what is produced by Doppler cooling in the experiment. For well #1:

$$a_i^2 = \frac{e^{-E_i/kT}}{q(T)}, \quad (30)$$

$$q(T) = \sum_i e^{-\frac{E_i}{kT}}, \quad (31)$$

where E_i is the energy of the local mode state, k is Boltzmann's constant, T is thermodynamic temperature (very low in the experiment), and q is the partition function. And similar for the well #2. The value of temperature T was tuned iteratively to reproduce the experimental value of the mean occupation in each well, as defined by Equation (27). For example, in order to mimic the
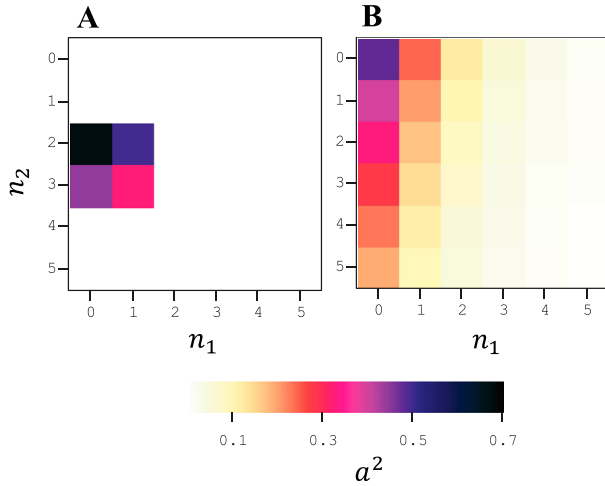
Figure 3. Initial populations of the local mode states in the Be^+ experiment obtained by two methods: (a) superposition of small number of close-lying states; (b) Boltzmann distribution of state populations.

Be^+ experiment we had to set $T_1 = 146\mu K$ for well #1 and $T_2 = 546\mu K$ for well #2. The resultant distribution of the initial state populations, determined as $a_{ij}^2 = a_i^2 a_j^2$, is illustrated by Figure 3(b). A comparison of Figure 3(a) with Figure 3(b) shows that the number of initially populated vibrational states is significantly larger and the most populated state is the ground vibrational state.

Note that if initial conditions are set up using the second method (thermal distribution of the initial states, rather than a coherent sum) then several independent calculations of the dynamics are required, for each initial local-mode eigenstate (i.e. each populated 'square' in Figure 3(b)):

$$\psi^{in}(\Delta z_1, \Delta z_2) = \varphi_i^{loc}(\Delta z_1)\varphi_j^{loc}(\Delta z_2). \quad (32)$$

The results of each calculation must be analysed independently, as discussed in Sec. 3.2 below, and the final result is obtained as an average, using the thermal distribution of weights a_{ij}^2.

The same two procedures were applied to mimic the initial conditions of the Ca^+ experiment. The first method gave $a_{40} = \sqrt{0.5}$ and $a_{09} = \sqrt{0.5}$. The second method resulted in $T_1 = 883\mu K$ and $T_2 = 1871\mu K$.

3.2. Wave packet analysis

At every time step we project the system's wave function $\psi^t(\zeta_1, \zeta_2)$ onto the eigenfunctions of the local vibrational modes:

$$a_{ij}^t = \langle \varphi_i^{loc}(\Delta z_1)\varphi_j^{loc}(\Delta z_2)|\psi^t(\zeta_1, \zeta_2)\rangle, \quad (33)$$

From these probability amplitudes the instantaneous occupations of the two wells, $\langle n_1^t \rangle$ and $\langle n_2^t \rangle$, can be computed as:

$$\langle n_1^t \rangle = \sum_i i \cdot \sum_j |a_{ij}^t|^2. \quad (34a)$$

$$\langle n_2^t \rangle = \sum_j j \cdot \sum_i |a_{ij}^t|^2. \quad (34b)$$

We performed calculations with 101 time steps up to $t = 800\mu s$ for the Be^+ experiment and up to $t = 1000\mu s$ for the Ca^+ experiment to obtain the dependence of mean occupation $\langle n_1 \rangle$ as a function of time on resonance. Figure 4 compares our results with experimental data. In both experiments, the value of the mean occupation for one of the wells $\langle n_1 \rangle$ changes periodically with time on resonance t, demonstrating that the ions in the two wells of the double-well trap swap their vibrational energy. More importantly, the amplitude of these swaps is quite significant. For example, in the case of Be^+ experiment, where the initial occupations are only $\langle n_1 \rangle = 0.35$ and $\langle n_2 \rangle = 2.3$, the amplitude of the swap is close to two, which means that the ions exchange *almost all* of their vibrational energy. In the Ca^+ experiment the ions swap close to 5 quanta of energy out of 9 excitation quanta available in the system. Although the experimental error bars are significant, particularly in the case of Be^+ experiment, the number of measurements (snapshots) is also large, which allows fitting experimental data by an analytic expression (see Equation (35) below and Appendix 1). Note that in both experiments a non-negligible heating of the system was observed, and the heating rates were measured and reported. We also added heating to the time-dependence of $\langle n_1^t \rangle$ presented in Figure 4, in an *ad hoc* way using experimental values of the rates, as explained in Appendix 1. This is similar to what was done in analysis of experimental results [19,20].

Figure 4 demonstrates that our results (dashed pink line) follow the fit of experimental data (solid blue line in the frame A and solid black line in the frame B) almost perfectly, for both Be^+ and Ca^+ experiments. Both the amplitude and the frequency of the vibrational energy exchange are well reproduced. Numerical values of the energy swap time τ_{swp} for each case is reported in Table 1, where the experimentally measured values of this important characteristic of the process are also given. To obtain the value of τ_{swp} from our calculations we fit the rigorously computed $\langle n_1^t \rangle$ dependence by a simple analytic expression that describes periodical swap of the vibrational energy between the ions:

$$\langle n_1^t \rangle = \langle n_1^0 \rangle \cos^2\left(\frac{\pi t}{2\tau_{swp}}\right) + \langle n_2^0 \rangle \sin^2\left(\frac{\pi t}{2\tau_{swp}}\right), \quad (35)$$
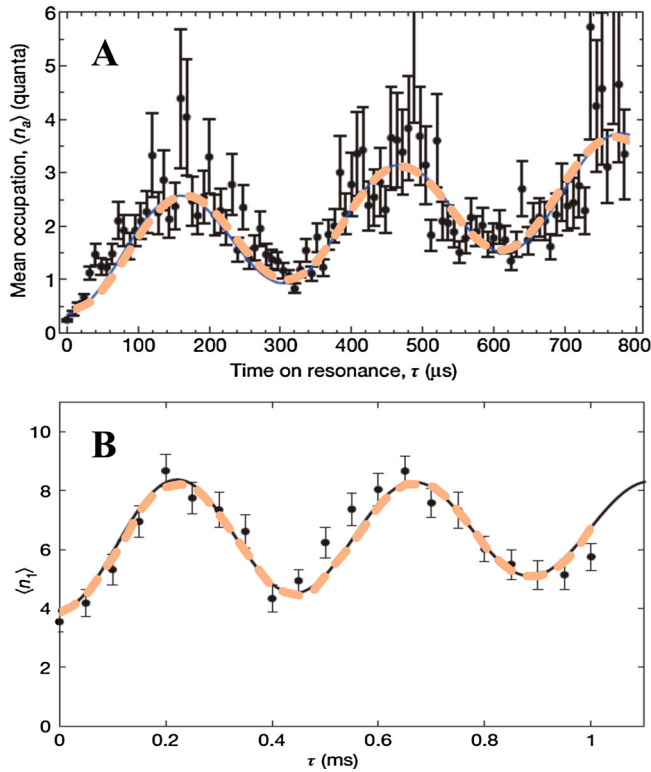
Figure 5. High-frequency low-amplitude oscillations of the mean occupation $\langle n_1 \rangle$ for the case of Be^+ experiment.

Figure 4. Vibrational energy swap between two ions in: (a) the Be^+ experiment [19]; (b) the Ca^+ experiment [20], as a function of time on resonance. Experimental error bars are indicated. Solid blue line on plot A and solid black line on plot B show the fits of experimental data. Pink dashed lines represent our computational results for each case. Experimental data are reprinted with permission from Macmillan Publishers Ltd: Nature, copyright (2011).

where the initial well occupations $\langle n_1^0 \rangle$ and $\langle n_2^0 \rangle$ and the exchange time τ_{swp} were the fitting parameters. For the Be^+ experiment we obtained $\tau_{swp} = 155.11\mu s$, while for Ca^+ experiment we obtained $\tau_{swp} = 222.25\mu s$. These values are very close to the experimental values of $155\mu s$ and $222\mu s$, respectively.

Interestingly, analysis of our results reveals a feature not described in the experimental papers. We found that in addition to the large-amplitude small-frequency swaps discussed above (Figure 4), there is also a higher-frequency lower-amplitude energy exchange process going on. This is illustrated by Figure 5 for the case of Be^+ experiment. From this picture one can see that the amplitude of this energy exchange process is only on order of 0.004 quanta, which would be impossible to identify in the experiment. The characteristic time-length of this process is $\sim 0.25\mu s$, which is on order of $10^{-3} \times 2\tau_{swp}$. This time-scale corresponds to the vibration period and characterises the *intra-well* wave packet dynamics, in contrast to the *inter-well* dynamics presented in Figure 4. On this time scale the vibrationaly
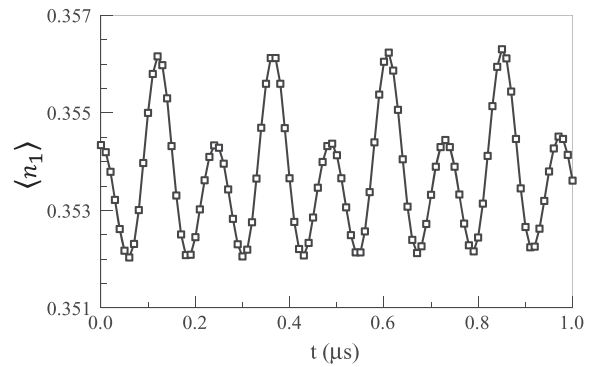
excited wave packet moves between the turning points on the PES and the real and imaginary parts of it evolve according to the phases acquired by its components.

We found that our set up of the initial conditions does not affect the energy swap dynamics, which is also quite interesting. On the time scale of Figure 4, two types of the initial conditions illustrated by Figure 3(a) and (b) lead to nearly identical time-dependencies of the average occupation $\langle n_1^t \rangle$, in spite of the fact that the underlying dynamics, in terms of time-dependence of state occupations, is very different. Figure 6 illustrates this feature, for the case of Be^+ experiment. Here we plotted separately the contribution of every state ($i = 0, 1, 2, 3, 4$ and 5) to the average value of $\langle n_1^t \rangle$. Namely, we plotted the time evolution of different terms in the sum over i in Equation (34a), after first summing each term over j and the result being pre-multiplied by the value of i. Two frames of Figure 6 correspond to two different initials conditions illustrated by the two frames of Figure 3. From this analysis we see clearly that although evolutions of state populations are very different in two cases (thin lines), the overall evolutions of average occupations $\langle n_1^t \rangle$ are nearly identical. The differences we found are very small, at the level of 0.005 quanta, which is indistinguishable at the scale of Figures 4 and 6. As a stress test, we also tried to vary the initial conditions and we found that all our results support the following conclusion: the distribution of state-populations at the initial moment of time does not affect time evolution of the average occupation $\langle n_1^t \rangle$. However, the initial value of $\langle n_1^0 \rangle$ does affect the *amplitude* of energy swaps. This finding may have some implications for the experimental studies of the process.

Figure 7 illustrates evolution of the accurate two-dimensional wave function of the system $\psi^t(\zeta_1, \zeta_2)$ in the Be^+ experiment on the time-scale of two swap times, $0 < t < 2\tau_{swp}$. The initial conditions of Figure 3(a) are used, which gives the initial wave packet presented in Figure 7(a). The nodal structure of this wave packet
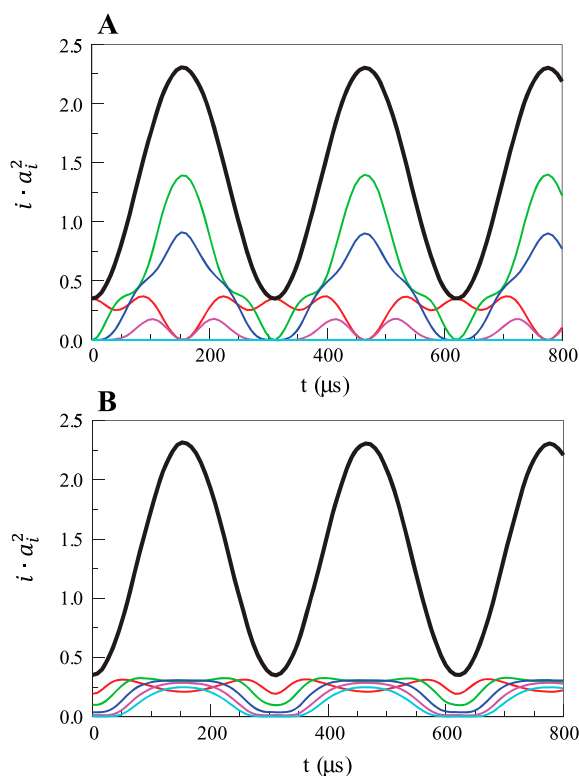
A

B

Figure 6. Evolution of average occupation (black) for the well #1 of the Be^+ system when the initial state was prepared by creating: (a) Coherent superposition of four vibrational states; (b) Incoherent thermal distribution of states; as indicated in Figure 3. Thin coloured lines represent contributions from five exited states to the mean occupation. Red, green, blue, magenta and cyan correspond to 1, 2, 3, 4 and 5 quanta of excitation, respectively. (Colour online.)

reveals the distribution of its energy over two local modes, rather than normal modes. The contour lines of the PES are also shown in Figure 7(a) (one contour line per $\hbar\omega_0$), and one can see that at this length scale the PES is nearly harmonic and symmetric. We can also see that the initial wave packet is significantly displaced from the minimum energy point. Five snapshots of $\psi^t(\zeta_1, \zeta_2)$ are shown in Figure 7(b). During its evolution the structure of wave function becomes unusually shaped and rather diffused, as one sees at $t = \tau_{swp}/2$ and at $t = 3\tau_{swp}/2$. At $t = \tau_{swp}$ the wave function is again simple, representing a mirror image of the initial wave packet and describing the state at which the local modes (or the wells) have exchanged their initial states (or excitations). At the final time $t = 2\tau_{swp}$ the wave function returns to its original shape, as excitation returns to the well #1.

In order to better visualise and understand this process, we created animation of evolution of the wave packet $\psi^t(\zeta_1, \zeta_2)$ during the characteristic time τ_{swp} for the Be^+ experiment. The video file is available for download from Supplementary Materials [25]. Two versions of the

process were monitored, that correspond to two choices of the initial conditions illustrated by Figures 3(a) (in the Movie 1) and (b) (in the Movie 2). Still, we should admit that, even after watching these movies it is hard to come out with simple interpretation for this behaviour. The time/space evolutions of the wave function in these movies is not intuitive. Why in Figure 7(b) at $t = \tau_{swp}/2$ and then at $t = 3\tau_{swp}/2$ the wave function acquires a half-donut-like shape? This becomes clear in the next section.

3.3. Other computational experiments

To identify the origin of the energy swaps we carried out several additional calculations. In one of these we set up idealised initial conditions, quite different from conditions of the experiments. Namely, we consider a situation in which one Be^+ ion has no excitation at all (i.e. in the ground vibrational state $i = 0$ with $\langle n_1 \rangle = 0$ exactly) while the other ion is highly excited, to an eigenstate $j = 10$ rather than to a superposition of states, so that $\langle n_2 \rangle = 10$ exactly. Analyzing evolution of $\psi^t(\zeta_1, \zeta_2)$ in this case we found that such choice of the initial conditions eliminates completely the low-amplitude high-frequency oscillations of the average well populations that correspond to the intra-well dynamics, like those presented in Figure 5. This makes sense, since eigenstates do not evolve in time. However, the energy swaps between the wells on the time-scale τ_{swp} have survived, and in this case, we observe a complete transfer of 10 quanta of excitation from one well to the other. This demonstrates once again that the choice of the initial conditions does not influence the energy swaps. Animation of the wave packet dynamics for this case is also available from the Supplementary Materials [25], in the Movie 3. Figure 8 gives several snapshots of the evolving wave function, which undergoes rather impressive evolution in this case. Being localised in the vicinity of Δz_2 at the initial moment of time, the wave function transforms into a donut at $t = \tau_{swp}/2$ (see Figure 8), after which it reassembles in the vicinity of Δz_1 at $t = \tau_{swp}$. It then transforms back into a donut at $t = 3\tau_{swp}/2$, and finally, at $t = 2\tau_{swp}$, it returns to its initial shape near Δz_2. Comparing Figure 7 with Figure 8 we find similarities, but in the case of Figure 8 the transformations are easier to see because of the specially chosen initial conditions. Still, the reason for this quite unusual behaviour remains unclear.

In the second computational experiment we eliminate the effect of *anharmonicities* in the system. For this we replace the accurately computed spectrum and wave functions by those obtained from the normal mode analysis. This is equivalent to approximating the PES by a 2D paraboloid, a harmonic system with two normal mode
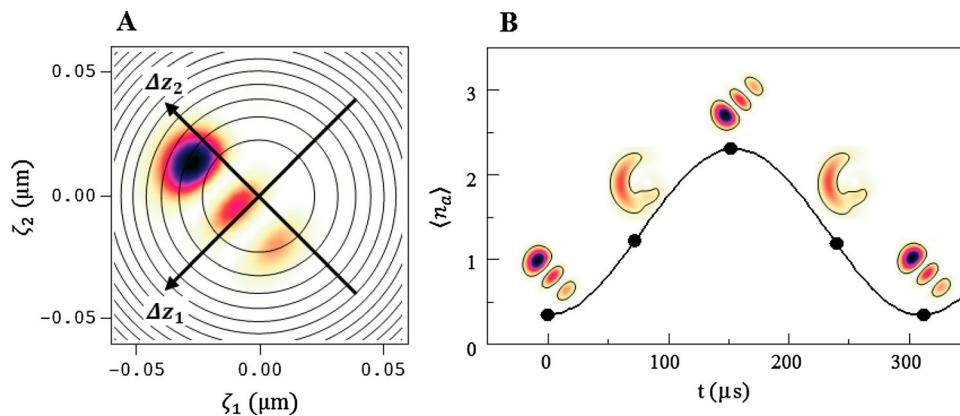
Figure 7. (a) Square modulus of the initial wave packet for the Be^+ system prepared as a superposition of small number of states, as illustrated by Figure 3(a). Contour lines represent the PES of the system; (b) Evolution of this wave packet over the time period $2\tau_{swp}$. Snapshots of wave function are taken at the points indicated by black dots.

frequencies ω_1 and ω_2 and an analytic wave function. In this case we still observe the inter-well energy swaps, characterised by basically the same value of τ_{swp}. This makes sense, since, as one can see from Table 3, the values of vibrational anharmonicities in the system are negligible, even when compared to the relatively small frequency splitting: $\Delta \approx \delta\omega \times 10^{-3}$, where $\delta\omega \approx \omega_{1,2} \times 10^{-3}$.

In the final numerical experiment, we eliminate the effect of *frequency splitting* $\delta\omega$, by setting $\omega_1 = \omega_2 = \omega_0$, using the corresponding degenerate energy spectrum and exactly the same wave functions for both normal modes. This is equivalent to approximating the PES by a rotating paraboloid. Our calculations show that this last change, finally, shuts-off the inter-well energy swaps. Since the swap time is the inverse of the frequency splitting $\delta\omega$ [19,20], this result can be interpreted as $\delta\omega = 0$ leads to an infinite τ_{swp}.

To understand this result better we computed evolution of a Gaussian wave packet for two idealised cases mentioned above: a perfectly symmetric well ($\omega_1 = \omega_2$) and a weakly asymmetric well ($\omega_1 \neq \omega_2$). In each case the shape of the initial Gaussian was equivalent to the ground vibrational state, while the displacement off the equilibrium position was chosen to give $\langle n_1 \rangle = 0$ exactly and a large value of $\langle n_2 \rangle \sim 12$. Figure 9 illustrates this choice, when the initial position of the Gaussian wave packet is in the upper left corner, on the axis Δz_2 (compare to Figure 7(a)). Again, this initial condition is quite different from that in the experiment, but it results in a simple evolution of the wave packet, which demonstrates the underlying principle. The dynamics is simple in this case because Gaussian wave packet in a harmonic potential remains localised during its evolution, and thus its motion can be easily interpreted by the means of a *classical trajectory*. Animation of such trajectory is available from the Supplemental Material [25] (the Movie 4)

and is explained below. We encourage readers to watch the animation prior to reading further. It shows that after several cycles of reflection the trajectory transforms from a straight line at $t = 0$ into a circle at $t = \tau_{swp}/2$, which explains the appearance of those donut-shaped wave functions in Figures 7 and 8.

Figure 9(a) explains the evolution of the Gaussian wave packet in the case of a perfectly symmetric well ($\omega_1 = \omega_2$). The wave packet starts in the upper left corner, moves to the centre of the well, then climbs up to the turning point (lower right corner), where it is reflected. Since the PES is perfectly round in this case, the wave packet is reflected straight back (along the diameter) and returns exactly to its initial location. This cycle repeats again and again, and the wave packet stays on the Δz_2 infinitely long. No motion along Δz_1 occurs which means that no energy is transferred to the other well, and the value of $\langle n_1 \rangle = 0$ remains unchanged.

Figure 9(b) explains evolution of the same initial Gaussian wave packet in the case of a slightly asymmetric well with $\omega_1 < \omega_2$. Asymmetry of the contour lines of the PES is exaggerated in Figure 9(b), for the purpose of clarity. Of importance is that the initial wave packet will follow the gradient of the PES, and its trajectory will start to deviate from the axis Δz_2, simply because in the case of $\omega_1 \neq \omega_2$ the contour lines are ovals, rather than circles (compare Figures 9(a) and (b)). When the wave packet hits its first turning point (in the lower right corner) it is reflected back towards its initial position. Notice that at the turning point the contour line of the PES is not perpendicular to the momentum vector. Even if one thinks classically, assuming that the angle of reflection equals to the angle of incidence, one concludes that the wave packet will not return to its original position, but to a slightly different point. Namely, its new position will be slightly above the axis Δz_2 (see
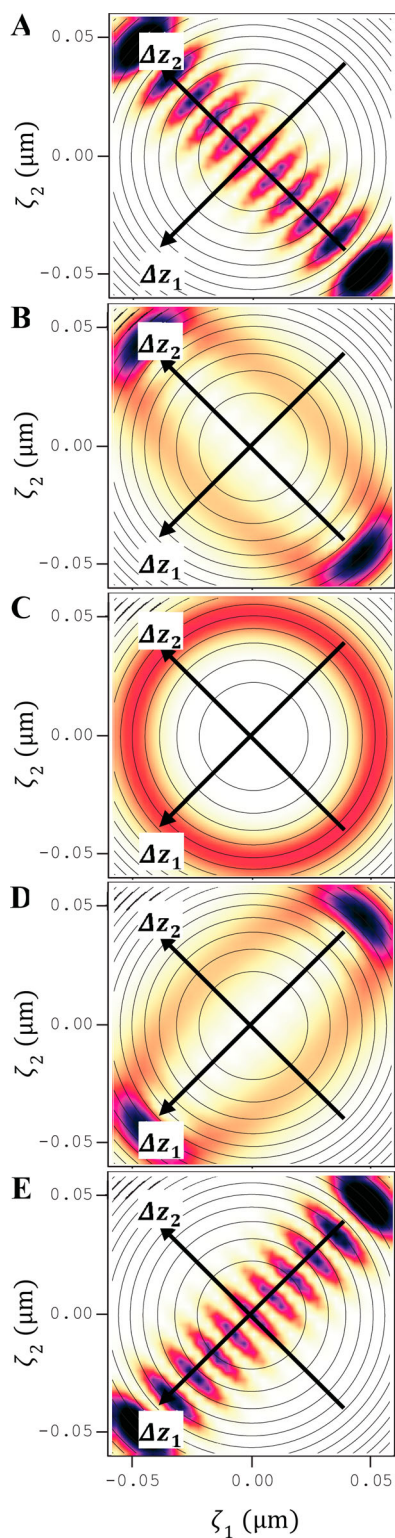
Figure 8. Several snapshots of wave packet evolution for the computational experiment with the initial state (0,10) that corresponds to significant excitation of the second ion, with the first ion being in its ground state. The snapshots show the square modulus of the wave packet. Snapshots B, C, D and E are taken at moments of time $\frac{1}{4}\tau_{swp}$, $\frac{1}{2}\tau_{swp}$, $\frac{3}{4}\tau_{swp}$ and τ_{swp}, respectively.
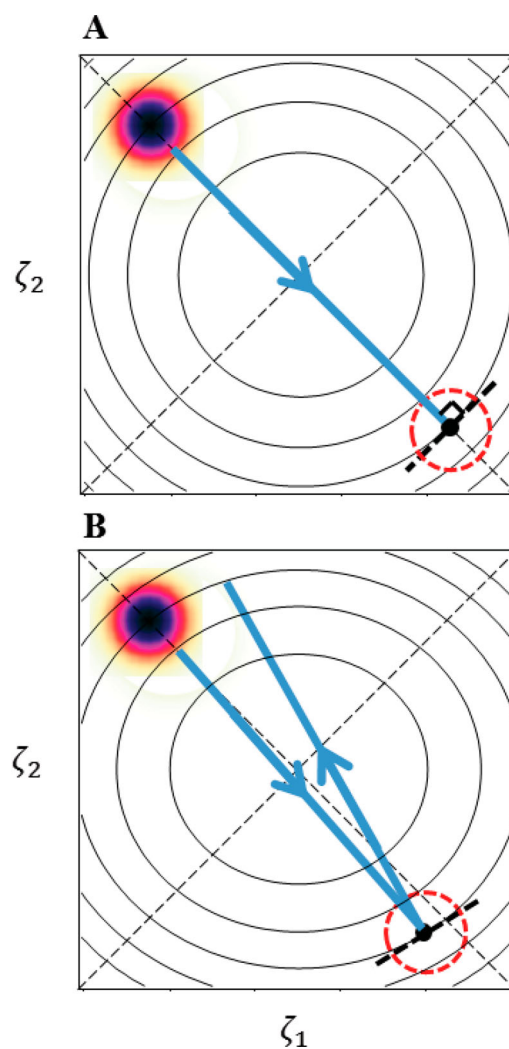

Figure 9. Explanation of the Gaussian wave packet dynamics in the cases of: (a) a perfectly symmetric well with $\omega_1 = \omega_2$; and (b) an asymmetric well with $\omega_1 \neq \omega_2$. Contour lines of the PES are shown schematically by thin lines. The local mode axis Δz_1 and Δz_2 are indicated by dashed lines along the diagonals of the (ζ_1, ζ_2)- space of the normal mode coordinates (compare to Figure 7(a)). The initial wave packet is shown by colour. Red dashed circle shows the wave packet at the time of its reflection at the turning point. Upper frame illustrates that trajectory of the wave packet remains restricted to the diagonal line (the axis Δz_2) because the contour lines are perpendicular to the incidence vector. Lower frame shows that trajectory deviates from the axis Δz_2 (towards another diagonal line, which is the axis Δz_1), due to potential gradient, and, when reflected back, does not return to the initial point.

Figure 9(b)), which corresponds to some motion along Δz_1, which also means some increase of $\langle n_1 \rangle$ and some energy transfer to the other well.

Notice that each reflection gives the wave packet some angular momentum with respect to the origin. As time passes the trajectory evolves from a nearly straight line (along axis Δz_2 at the initial moment of time) into an

elliptic orbit in the $(\Delta z_1, \Delta z_2)$-space, with the longer principal axis positioned along Δz_2, and the shorter axis positioned along Δz_1. Figure 9(b) suggests that the wave packet follows this orbit in the counter clockwise direction. When time reaches $t = \tau_{swp}/2$ the orbit becomes perfectly circular, after which, it starts to lose the angular momentum (again, due to the classical reflection principle), transforming into an elliptical orbit. Now the longer principal axis lies along Δz_1, and the shorter axis lies along Δz_2. When time reaches $t = \tau_{swp}$ this ellipse degenerates into a nearly straight line along Δz_1. Because all the angular momentum is lost, a complete energy transfer occurs between the wells. Then the process plays back, with the wave packet rotating clockwise.

Since the frequency difference in the system is very small, $\delta\omega \approx \omega_{1,2} \times 10^{-3}$, the asymmetry of the PES is also very small. One reflection of the wave packet makes very little change. It takes more than 10^3 reflection cycles to 'turn' the trajectory by 90°, from the axis Δz_2 at $t = 0$ to the axis Δz_1 at $t = \tau_{swp}$, which means that the energy transfer is *very inefficient*. The origin of this phenomenon is in the well-known classical principle: the angle of reflection equals to the angle of incidence.

4. Conclusions

We proposed a rigorous computational treatment for quantum dynamics of cold ions in a double-well trap using a numerically accurate approach, without making any assumptions concerning the coupling strength between the ions, and without involving the harmonic approximation for energy spectrum of the system. The goal was to reproduce, from first principles, the process of energy swaps between two wells observed in the experiments at NIST [19] and Innsbruck [20]. The model parameters were carefully chosen to mimic experimental conditions. Vibrational anharmonicities, due to the combination of Coulomb interaction and a strongly anharmonic trapping potential, were accurately computed and were found to be very small, which is explained by the small amplitude of the vibrational motion of the ions. Experimental results of both NIST and Innsbruck groups were reproduced in detail. In addition, we provide new insight by analyzing the wave packet motion and the time-evolution of state populations. We show that the energy swaps are basically a classical phenomenon that can be understood using the principle of trajectory reflection, at least for the localised initial wave packets. A rigorous solution of time-dependent Schrodinger equation supports this interpretation.

The model developed in this work can be used to study theoretically the new experiments at NIST [26,27]. It can also help to explore new schemes for the coherent and optimal control of the ionic motion in the double-trap architectures [28,29]. For example, one could computationally test various possible shapes of the double-well trap potential, as alternative to the simplest shape of Equation (1), with the goal of identifying the architectures that possess some desirable properties, such as increased or suppressed efficiency of the energy swaps between the wells. One may also think of adding an additional control field to the trap, in order to alter the effective barrier height between the wells, which would result in the modified properties of the spectrum (anharmonicities, and the detuning $\delta\omega$). Moreover, such control field could be made time-dependent and shaped optimally for maximising the probabilities of certain state-to-state transitions, and minimising the others [21,22]. These aspects will be addressed in the future work.

Disclosure statement

No potential conflict of interest was reported by the authors.

References

[1] D.J. Larson, J.C. Bergquist, J.J. Bollinger, W.M. Itano and D.J. Wineland, Phys. Rev. Lett. **57**, 70 (1986).
[2] J.I. Cirac and P. Zoller, Phys. Rev. Lett. **74**, 4091 (1995).
[3] R. Blatt and D. Wineland, Nature **453**, 1008 (2008).
[4] H. Häffner, C.F. Roos and R. Blatt, Phys. Rep. **469**, 155 (2008).
[5] J.D. Jost, J.P. Home, J.M. Amini, D. Hanneke, R. Ozeri, C. Langer, J.J. Bollinger, D. Leibfried, D.J. Wineland, Nature 459, 683 (2009).
[6] R. Islam, E.E. Edwards, K. Kim, S. Korenblit, Noh C., Carmichael H., Lin G.-D., Duan L.-M., Joseph Wang C.-C., Freericks J.K., Monroe C., Nature Commun. 2, 377 (2011).
[7] K. Kim, S. Korenblit, R. Islam, E.E. Edwards, M.-S. Chang, C. Noh, H. Carmichael, G.-D. Lin, L.-M. Duan, C.C. Joseph Wang, J.K. Freericks, C. Monroe, New J. Phys. 13, 105003 (2011).
[8] A. Steane, Appl. Phys. B. 64, 623 (1997).
[9] S. Gulde, M. Riebe, G.P.T. Lancaster, C. Becher, J. Eschner, H. Häffner, F. Schmidt-Kaler, I.L. Chuang, R. Blatt, Nature 421, 48 (2003).

[10] D. Leibfried, B. DeMarco, V. Meyer, D. Lucas, M. Barrett, J. Britton, W.M. Itano, B. Jelenković, C. Langer, T. Rosenband, D.J. Wineland, Nature 422, 412 (2003).

[11] J. Benhelm, G. Kirchmair, C.F. Roos and R. Blatt, Nat. Phys. **4**, 463 (2008).

[12] J.P. Home, D. Hanneke, J.D. Jost, J.M. Amini, D. Leibfried and D.J. Wineland, Science **325**, 1227 (2009).

[13] D.J. Wineland, Phys. Scr. 2009, 014007 (2009).

[14] D. Hanneke, J.P. Home, J.D. Jost, J.M. Amini, D. Leibfried and D.J. Wineland, Nat. Phys. 6, 13 (2010).

[15] J.I. Cirac and P. Zoller, Nature 404, 579 (2000).

[16] D. Kielpinski, C. Monroe and D. Wineland, Nature 417, 709 (2002).

[17] J.M. Amini, H. Uys, J.H. Wesenberg, S. Seidelin, J. Britton, J.J. Bollinger, D. Leibfried, C. Ospelkaus, A.P. VanDevender, D.J. Wineland, New J. Phys. 12, 033031 (2010).

[18] C. Monroe and J. Kim, Science **339**, 1164 (2013).

[19] K.R. Brown, C. Ospelkaus, Y. Colombe, A.C. Wilson, D. Leibfried and D.J. Wineland, Nature 471, 196 (2011).

[20] M. Harlander, R. Lechner, M. Brownnutt, R. Blatt and W. Hansel, Nature 471, 200 (2011).

[21] L. Wang and D. Babikov, Phys. Rev. A 83, 022305 (2011).

[22] L. Wang and D. Babikov, Phys. Rev. A 83, 052319 (2011).

[23] W. Press, S. Teukolsky, W. Vetterling and B. Flannery, *Numerical Recipes in Fortran 90* (Cambridge University Press, New York, 1996).

[24] E. Anderson, Z. Bai, C. Bischof, S. Blackford, J. Demmel, J. Dongarra, J. Du Croz, A. Greenbaum, S. Hammarling, A. McKenney and D. Sorensen, *LAPACK Users' Guide* (Society for Industrial and Applied Mathematics, Philadelphia, 1999).

[25] See Supplemental Material at [URL] for animations of the wave packet dynamics in the Be^+ double-well experiment.

[26] T.R. Tan, J.P. Gaebler, R. Bowler, Y. Lin, J.D. Jost, D. Leibfried and D.J. Wineland, Phys. Rev. Lett. **110**, 263002 (2013).

[27] A.C. Wilson, Y. Colombe, K.R. Brown, E. Knill, D. Leibfried and D.J. Wineland, Nature 512, 57 (2014).

[28] M. Zhao and D. Babikov, Phys. Rev. A 77, 012338 (2008).

[29] L. Wang and D. Babikov, J. Chem. Phys. 137, 064301 (2012).

[30] D.A. Hite, Y. Colombe, A.C. Wilson, D.T.C. Allcock, D. Leidfried, D.J. Wineland and D.P. Pappas, MRS Bull. 38, 826 (2013).

[31] M. Brownnutt, M. Kumph, P. Rabl, and R. Blatt, Rev. Mod. Phys. **87**, 1419 (2015).

[32] J.A. Sedlacek, A. Greene, J. Stuart, R. McConnell, C.D. Bruzewicz, J.M. Sage, and J. Chiaverini, Phys. Rev. A 97, 020302 (2018).

Appendix 1: Including the heating rates of the trap

In the Be^+ experiment at NIST [19] the vibrational energy exchange between the wells was accompanied by a linear growth of the mean occupation with time, due to the heating of the ions. This heating was included in the expression that was used to fit the experimental data as follows:

$$\langle n_1^t \rangle_{\exp} = \langle n_1^0 \rangle \cos^2(\Omega_{swp}t) + \langle n_2^0 \rangle \sin^2(\Omega_{swp}t) + \langle \dot{n} \rangle t, \quad (A1)$$

where $\langle \dot{n} \rangle$ is the heating rate for both wells and $\Omega_{swp} = \pi/2\tau_{swp}$ is experimental swap frequency. The fit of experimental data was done with four free parameters: the initial average occupations of two wells $\langle n_1^0 \rangle$ and $\langle n_2^0 \rangle$, the exchange frequency Ω_{swp} and the heating rate $\langle \dot{n} \rangle$. The value of the heating rate obtained from the fit was $\langle \dot{n} \rangle = 1,885$ quanta per second.

In our calculations the heating of the ions cannot be directly included in the time propagation of the wave function of the system. We can mimic the experiment by computing:

$$\langle n_1^t \rangle_{\exp} = \langle n_1^t \rangle + \langle \dot{n} \rangle t, \quad (A2)$$

where $\langle n_1^t \rangle$ is the result of our calculations without heating, as defined by Equation (36a) and fitted by Equation (37), and $\langle \dot{n} \rangle$ is the experimental heating rate. This moiety, $\langle n_1^t \rangle_{\exp}$, was computed and presented in Figure 4(a) for comparison with experimental results.

Likewise, the heating of the ions was observed in the Ca^+ experiments in Innsbruck [20] with the heating rate of $\langle \dot{n} \rangle = 1.3$ quanta per millisecond. But in addition, their data were also affected by the exponential damping of the energy swap efficiency with time. Their fitting expression included both these factors as follows:

$$\langle n_1^t \rangle_{\exp} = \langle n_1^0 \rangle + \frac{1}{2}(\langle n_2^0 \rangle - \langle n_1^0 \rangle)(1 - \cos(2\Omega_{swp}t))e^{-t/\tau_{dmp}}$$
$$+ \langle \dot{n} \rangle t, \quad (A3)$$

where τ_{dmp} is the damping constant. The value of this parameter obtained from the fit of experimental data was $\tau_{dmp} = 3$ms.

Expression (A3) can be rewritten as follows:

$$\langle n_1^t \rangle_{\exp} = \langle n_1^0 \rangle + (\langle n_2^0 \rangle - \langle n_1^0 \rangle)\sin^2(\Omega_{swp}\tau)e^{-t/\tau_{dmp}} + \langle \dot{n} \rangle \tau$$
$$= (\langle n_1^0 \rangle \cos^2(\Omega_{swp}t) + \langle n_2^0 \rangle \sin^2(\Omega_{swp}t))e^{-t/\tau_{dmp}}$$
$$+ \langle n_1^0 \rangle(1 - e^{-t/\tau_{dmp}}) + \langle \dot{n} \rangle \tau. \quad (A4)$$

From Equation (A4) we see that we can take into account both damping and heating terms as follows:

$$\langle n_1^t \rangle_{\exp} = \langle n_1^t \rangle e^{-t/\tau_{dmp}} + \langle n_1^0 \rangle(1 - e^{-t/\tau_{dmp}}) + \langle \dot{n} \rangle t. \quad (A5)$$

Again, here $\langle n_1^t \rangle$ is the result of our calculations without heating, as defined by Equation (36a) and fitted by Equation (37), while $\langle \dot{n} \rangle$ is the experimental heating rate and τ_{dmp} is the experimental damping constant. This moiety $\langle n_1^t \rangle_{\exp}$ corresponds to the Innsbruck experiment. It was presented in Figure 4(b) for comparison with experimental results.

The issue of noise in the ionic trap [30–32] was not covered in this work in detail. In the future, a simulation in Liouville space with Lindblad approximation could be implemented in order to account for the noise.